ADVANCED ENERGY MATERIALS
www.advenergymat.de

Triggering C–N Coupling on Metal Oxide Nanocomposite for the Electrochemical Reduction of CO_2 and NO_x^- to Formamide

Putri Ramadhany, Thành Trần-Phú, Jodie A. Yuwono, Zhipeng Ma, Chen Han, Thi Kim Anh Nguyen, Josh Leverett, Priyank Kumar, Rosalie K. Hocking, Antonio Tricoli, Alexandr N. Simonov, Rose Amal,* and Rahman Daiyan**

The co-electroreduction of CO_2 and NO_x^- (NO_3^-/NO_2^-) to generate formamide ($HCONH_2$) offers an opportunity for downstream chemical and polymer manufacturing decarbonization; however, significant challenges lie in the C–N coupling and the associated low product selectivity. Herein, *p*-block metal oxides are incorporated in copper oxides to provide more accessible active sites for reactant adsorption and activation, tuning the reaction selectivity toward the formamide production. Through in situ Raman and synchrotron-based infrared spectroscopy measurements, C—N bond formation is demonstrated in real-time with the CuO_x/BiO_x catalyst, where the C—N bond is detected via a *CHO and $*NH_2$ intermediates formation, in agreement with the density functional theory calculations. When tested in a flow electrolyzer, a formamide yield rate of 134 ± 11 mmol h^{-1} g_{cat}^{-1} is reported, the first report of co-electroreduction of CO_2 and NO_x^- to formamide beyond conventional H-cell measurements. These new insights on the C–N coupling mechanisms and scale-up capability provide directions for further development of electrocatalysts for the formamide production.

1. Introduction

Mitigating global climate change requires immediate technology transition, specifically targeted at reducing the carbon footprint of hard-to-abate industries, such as fertilizer and plastic production. One emerging pathway for deep-rooted decarbonization is the electrochemical CO_2 reduction reaction (CO_2RR), which can be powered using renewable energy, to convert anthropogenic emissions of CO_2 into value-added chemical products. At present, CO_2RR to single-carbon products, such as CO and formate ($HCOO^-$), has demonstrated high selectivity and yield.[1] Generating higher carbon ($\geq C_{2+}$) products, such as ethanol and ethylene, is also possible with high selectivity (>80%) through the optimization of electrolyte conditions and catalyst design, despite the complexity of the C—C bond formation.[2]

CO_2 can be further coupled with nitrogenous small compounds such as nitrate/nitrite (i.e., NO_3^-/NO_2^- or collectively referred to as NO_x^- below) through electrochemical C—N bond formation to generate urea, amines, and amides (for use in fertilizer, fine chemicals, and pharmaceutical industries).[3] It is projected that the amine and amide

P. Ramadhany, Z. Ma, C. Han, J. Leverett, P. Kumar, R. Amal
Particles and Catalysis Research Laboratories and School of Chemical Engineering
UNSW Sydney
Sydney, NSW 2052, Australia
E-mail: r.amal@unsw.edu.au

T. Trần-Phú
Chemistry and Nanoscience Center
National Renewable Energy Laboratory
Golden, CO 80401, USA
E-mail: thanh.tran@nrel.gov

The ORCID identification number(s) for the author(s) of this article can be found under https://doi.org/10.1002/aenm.202401786

DOI: 10.1002/aenm.202401786

J. A. Yuwono
School of Chemical Engineering
The University of Adelaide
Adelaide, SA 5005, Australia

T. K. A. Nguyen, A. Tricoli
Nanotechnology Research Laboratory
The Sydney University
Sydney, NSW 2050, Australia

R. K. Hocking
School of Science
Swinburne University of Technology
Melbourne, VIC 3122, Australia

A. N. Simonov
School of Chemistry
Monash University
Melbourne, VIC 3800, Australia

R. Daiyan
Particles and Catalysis Research Laboratories and School of Minerals and Energy Resources Engineering
UNSW Sydney
Sydney, NSW 2052, Australia
E-mail: r.daiyan@unsw.edu.au

market will grow to $23 and $76 billion by 2030, respectively, while the fertilizer market is projected to reach $268 billion over the next five years, highlighting the global demand for these chemicals.[4] Supporting this demand through environmentally sustainable chemical synthesis will strongly assist in reducing the carbon footprint of these industries. However, the direct formation of C—N bonds through the co-electroreduction of CO_2 with NO_x^- presents the inherent challenge of low yields and product selectivity.[5] The immediate objective entails the refinement of electrocatalyst design to enhance the selective production of C—N products.

Key challenge for C—N coupling arise from the requirement of multiple complex reduction reactions, i.e., the CO_2RR and the electrochemical reduction of NO_x^- (NO_x^-RR), as well as the high number of electron transfers required.[6] For example, the formamide ($HCONH_2$) formation from the co-electroreduction of CO_2 and NO_3^- requires a transfer of 9 electrons.[7] Moreover, the reaction competes with the hydrogen evolution reaction (HER) as well as with the individual electrochemical reduction of CO_2 and NO_x^-, leading to complex product distributions and low faradaic efficiency (FE) for the desired product.[5,6b] A range of catalyst design strategies, targeting enhanced chemisorption for the C—N intermediates and suppressing the HER, including defect engineering,[8] confining metal active sites to single and dual atoms to control reaction selectivity,[9] or the frustrated Lewis pair strategy,[10] have been proposed and explored. Nonetheless, there is still a lot of room for improvements in the yield rates and selectivity to enable scale-up and, eventually, commercialization of these technologies.

Cu is known to provide moderate binding energy for carbon species, a characteristic that facilitates the retention of surface intermediates during CO_2RR, thereby promoting the C–C coupling.[5,11] Cu also has the highest occupied molecular orbital (HOMO) similar to the lowest unoccupied molecular orbital (LUMO) of NO_3^-, thereby promoting NO_3^- reduction to NO_2^-.[12] Moreover, recent reports have highlighted the potential of Cu-based catalysts to facilitate the C—N coupling during the CO_2 and NO_x^- co-electroreduction,[9b,13] which might be associated with similar physicochemical properties between C and N atoms as well as weak ability of Cu to adsorb hydrogen.[7] For example, commercially available Cu nanoparticles were reported to catalyze the electrochemical acetamide and formamide production, attaining a FE of 38% and 0.4% at −0.68 and −0.58 V versus reversible hydrogen electrode (RHE), respectively, *albeit* lacking information of yield rate.[5,14] Oxide-derived Cu nanoparticles were suggested to enable the ethylamine electrosynthesis but with a very low FE of 0.3% at −1.0 V versus RHE.[6a] Recently, we have reported the ability of Cu single atoms to generate urea from CO_2 and NO_3^- with an FE and yield rate of 28% and 30 mmol h^{-1} g_{cat}^{-1}, respectively, provided by the Cu—N_4 active sites.[9b]

Despite showing promise for a range of C—N coupling products, the primary drawbacks of the monometallic Cu catalysts reported to date include slow reaction kinetics,[15] low yield and selectivity that complicates separation of the desired product[5], and poor stability due to Cu dissolution.[14,16] In an attempt to overcome this, Cu has been combined with noble metals such as Pd, Au, Rh, or Ru to promote the C—N coupling, though with limited success, owing to competing reactions.[17] To bring the performance of the Cu catalysts for the C—N coupling reactions closer to the level of the CO_2RR, a deeper understanding of both the C—N coupling mechanism and the underlying catalyst structure-activity relationships is required.

In this work, we explore the effect of combining *p*-block metal oxides, BiO_x and SnO_x, with CuO_x as a strategy to provide dual active sites for the reactant adsorption and activation, directing the selectivity toward the targeted C—N product (**Figure 1a**).[18] The *p*-block metals have poor activity for HER as is their reasonable activity for the CO_2RR-to-$HCOO^-$, which has been demonstrated decades ago and proven through numerous studies.[18b,19] Subsequently, addition of *p*-block metals could lead to the formation of *CHO intermediates, which is hypothesized to be the key intermediate for the formamide production.[7] Conversely, Cu and its oxides were reported to promote the reduction of NO_x^- to $*NH_2$ and facilitate the C—N coupling between *CHO and $*NH_2$.[7,13,18c] Through the use of a comprehensive suite of experimental characterization techniques and density functional theory (DFT) calculations, we demonstrate that the combination of BiO_x and CuO_x nanoparticles facilitates a continuous relay of two-step process for formamide generation from CO_2 and NO_x^-. Leveraging the promising performance of the CuO_x/BiO_x system, we present, to the best of our knowledge, the pioneering study of co-electroreduction of CO_2 and NO_x^- to formamide in a flow electrolyzer.

2. Results and Discussion

2.1. Activity for the CO_2RR, NO_x^-RR, and C—N Coupling

The CuO_x, BiO_x, SnO_x, CuO_x/SnO_x, and CuO_x/BiO_x materials were directly deposited onto carbon-fiber paper (CFP) electrodes by a scalable flame spray pyrolysis (FSP), which enables the formation of porous monoclinic, tetragonal, and cassiterite crystal structures for CuO_x, BiO_x, and SnO_x, respectively, as reported by us and others (Figures S1–S6, Supporting Information).[18b,c,20] The CuO_x/BiO_x and CuO_x/SnO_x are the combinations of CuO_x-BiO_x and CuO_x-SnO_x particles mixed at the nanoscale with no evidence for the formation of solid solutions and bimetallic compounds according to the X-ray absorption spectroscopy (XAS) analysis discussed below.

The CuO_x, BiO_x, and SnO_x materials were first tested for NO_3^-RR (Figure 1b) and CO_2RR (Figure 1c) in a conventional three-electrode configuration using a two-compartment cell filled with either CO_2- or Ar-saturated aqueous 0.1 M $KHCO_3$ with or without 0.05 M KNO_3 added. The cyclic voltammetry (CV) curves (Figure S7, Supporting Information) indicate that the addition of BiO_x and SnO_x to CuO_x does not significantly increase the current density (*j*) during NO_3^-RR or CO_2RR. A similar trend for the FE and yield rate of NH_4^+ was also observed during fixed potential electrolysis (Figure 1b), indicating that CuO_x is more active in the NO_3^- reduction to NH_4^+ than *p*-block metal oxides. The maximum NH_4^+ yield rate of 261 ± 3 mmol h^{-1} g_{cat}^{-1} (130 ± 2 µmol h^{-1} cm^{-2}; hereinafter, per geometric surface area of the electrode) is achieved for the CuO_x catalyst at −1.0 V versus RHE, which is comparable to the activity of CuO_x for the NO_3^-RR to NH_4^+ reported by others.[18c] The main CO_2RR products for CuO_x are formate and CO, with a maximum FE_{HCOO^-} and FE_{CO} of 52.6 ± 0.3% and 18.2 ± 0.1%, respectively, achieved at −1.0 V versus

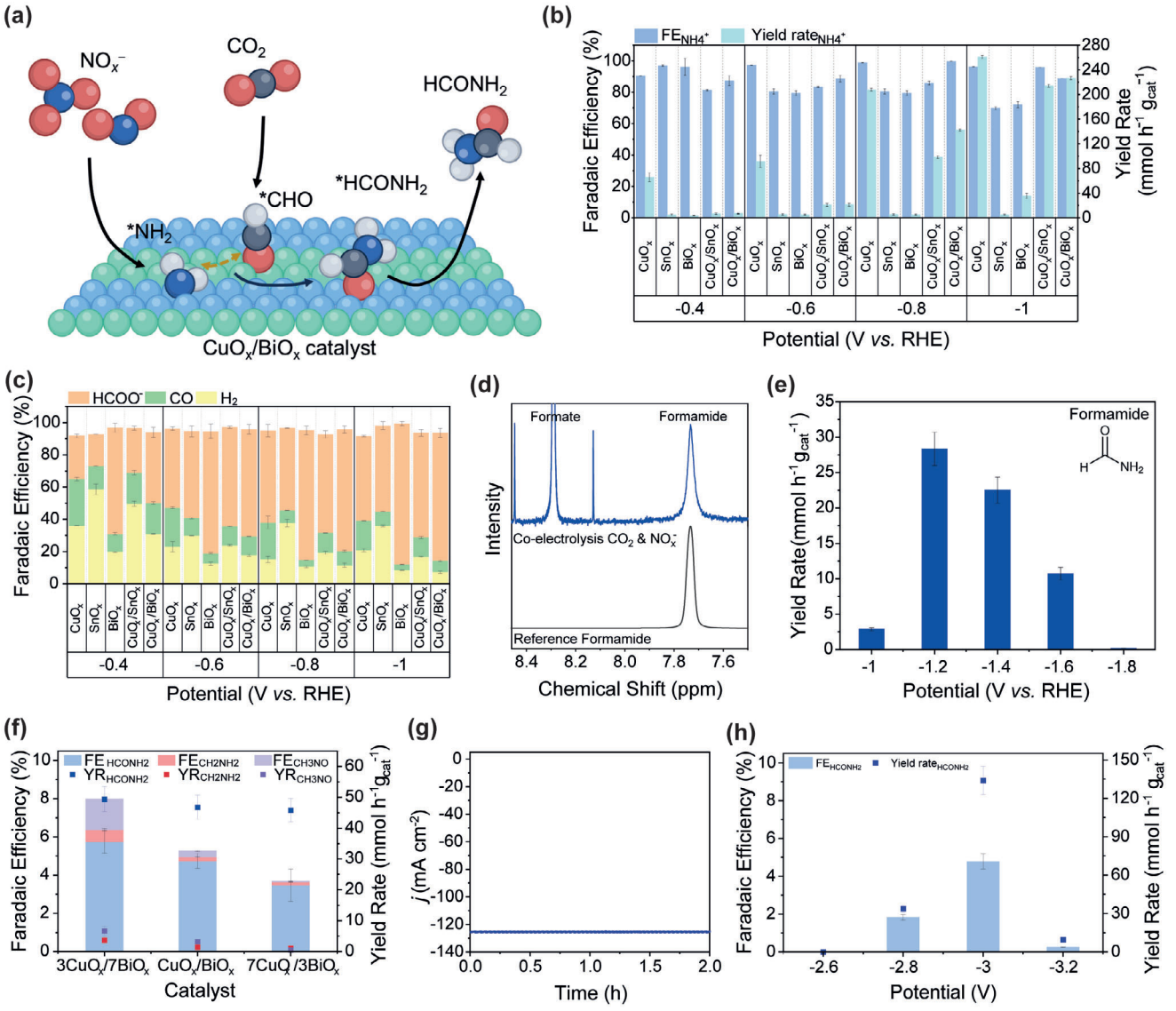

Figure 1. The effect of *p*-block oxides on the CuO_x activity for formamide electrosynthesis: a) A hypothesized mechanism of the formamide production from co-electroreduction of CO_2 and NO_x^-. b) The FE and yield rate of NH_4^+ during NO_3^-RR in Ar-saturated 0.1 M $KHCO_3$ and 0.05 M KNO_3 solution. c) The FE_{CO} and FE_{HCOO^-} during the CO_2RR in CO_2-saturated 0.1 M $KHCO_3$ solution. d) A representative ^{1}H NMR spectrum showing $HCONH_2$. e) The yield rate of formamide using CuO_x/BiO_x catalyst in CO_2-saturated 0.1 M $KHCO_3$ and 0.05 M KNO_3 solution. f) The FE and yield rate of formamide using different (y)CuO_x/(1-y)BiO_x catalysts at −1.2 V versus RHE. g) The steady state *j* at −3.0 V in a flow electrolyzer using CuO_x/BiO_x catalyst. h) The FE and yield rate of formamide in a flow electrolyzer for 2 h. Experiments in panels f-h used CO_2-saturated 0.2 M $KHCO_3$ + 0.02 M KNO_2 catholyte solution. Currents are normalized to the geometric surface area of the electrodes (1 cm^2), which were modified with 0.5 mg cm^{-2} of catalysts.

RHE (Figure 1c). The addition of *p*-block metal oxides BiO_x and SnO_x into CuO_x improves the FE_{HCOO^-} (Figure 1c), possibly due to the improved adsorption of the *HCOO intermediate.[1a,18a] At −1.0 V versus RHE, the maximum FE_{HCOO^-} for CuO_x, SnO_x, BiO_x, CuO_x/SnO_x, and CuO_x/BiO_x, are 52.6 ± 0.3%, 51 ± 2%, 87.2 ± 1.3%, 65 ± 2%, and 79 ± 3%, respectively, which are also comparable to the previously reported results.[1c,19a,20,21]

Further, we explored the co-electroreduction of CO_2 and NO_3^- at −1.0 V versus RHE in a CO_2-saturated 0.1 M $KHCO_3$ + 0.05 M KNO_3 solution. CuO_x and CuO_x/BiO_x catalysts (Figure S8, Supporting Information) were found to generate formamide, as detected using ^{1}H NMR (Figure 1d), with the yield rates of 1.4 ± 0.2 and 2.8 ± 0.3 mmol h^{-1} g_{cat}^{-1} (0.7 ± 0.1 and 1.4 ± 0.1 μmol h^{-1} cm^{-2}), respectively (Figure S9a–c, Supporting Information). The catalysts were then tested across a wider potential range (Figures S9d and S10c, Supporting Information), with CuO_x/BiO_x exhibiting higher formamide yield rate compared to CuO_x. Under examined conditions, the fastest generation of $HCONH_2$ with CuO_x/BiO_x, viz. 28 ± 3 mmol h^{-1} g_{cat}^{-1} (14 ± 2 μmol h^{-1} cm^{-2}), was achieved at −1.2 V versus RHE (Figure 1e), *albeit* with low faradaic efficiency of <1%. The major products detected include formate, CO, and NH_4^+ (Figure S10a,b, Supporting Information), which would compete significantly with the desired C—N coupling reaction.[5] We also find

that more negative potentials lead to a decline in the formamide yield rate and FE due to the enhanced HER kinetics (Figure S10a, Supporting Information). Moreover, we investigate the selectivity of formamide in relation to reaction time (Figure S10d, Supporting Information). Our findings indicate that extending the reaction beyond 12 h does not necessarily enhance the selectivity for formamide, due to the competing HER and CO_2RR producing methanol and acetate, respectively.

2.2. Optimization and Scale-Up of the Formamide Generation

Further, we explored the role of the electrolyte in the efficiency of C–N coupling for the formamide generation. A solution of 0.1 M $KHCO_3$ and 0.05 M KNO_3 served as the reference basis. Increasing the $KHCO_3$ concentration from 0.1 to 0.2 M was found to enhance *j* (Figure S11, Supporting Information), FE of formamide from 0.36 ± 0.02 to 0.50 ± 0.06%, as well as the formamide yield rate from 3.0 ± 0.3 to 5.0 ± 0.5 mmol h^{-1} g_{cat}^{-1} (Figure S12a, Supporting Information) at −1.0 V versus RHE. Similar trends were reported in the literature for both NO_3^-RR and CO_2RR.[18a,22] Specifically, HCO_3^- is a pH buffer that enhances the dissolution of CO_2 due to the equilibrium exchange between two species,[23] while the high concentration of K^+ facilitates the activation of NO_3^- and CO_2, followed by stabilization of their intermediates.[22a,24] However, further increasing the $KHCO_3$ concentration to 0.5 M leads to higher selectivity toward the HER and CO_2RR (Figure S13, Supporting Information), which could be attributed to the increase of local pH, improving CO_2 adsorption as well as direct bicarbonate reduction to generate hydrogen.[24b,25] Interestingly, lowering the NO_3^- concentration from 0.05 to 0.02 M improves formamide yield rate and FE to 8.0 ± 0.7 mmol h^{-1} g_{cat}^{-1} and 0.7 ± 0.1%, respectively (Figure S12b, Supporting Information). High NO_3^- concentrations can improve the diffusion rate and direct selectivity toward ammonium.[26] However, in the CO_2 and NO_3^- co-electroreduction, we hypothesized that there is a competition between reactants adsorption, which affects the available active sites and product distribution in an intricate manner. Replacing NO_3^- with NO_2^- significantly improves the C—N coupling that might be attributed to the lower overpotentials necessitated for the reduction of NO_2^- compared to NO_3^- (Figure S12c, Supporting Information), allowing prior reactant to be easily reduced as reported by previous studies.[27] Furthermore, a similar pattern to that observed with NO_3^- was also noted when varying the concentration of NO_2^-. The maximum FE and yield rate of formamide were achieved at a concentration of 0.2 M, as shown in Figure S12d (Supporting Information). As a result, combining the aforementioned strategies, a significantly improved formamide yield rate of 47 ± 4 mmol h^{-1} g_{cat}^{-1} (23 ± 2 μmol h^{-1} cm^{-2}) and FE of 4.8 ± 0.4% were achieved at −1.0 V versus RHE in CO_2-saturated 0.2 M $KHCO_3$ and 0.02 M KNO_2 solution (Figure S12c, Supporting Information).

We then explored the effect of the ratio between Cu and Bi in the bimetallic catalyst ((y)CuO_x/(1-y)BiO_x where y = 0.3, 0.5, and 0.7) on the FE and yield rate of formamide. Increasing the Bi fraction leads to an increase in the overall reduction rate (Figure S14, Supporting Information), as well as FE for formamide (Figure 1f). The conversion of CO_2 to *CHO is comparatively sluggish in comparison to NO_2^- to $*NH_2$ process (Figure S10d, Supporting Information), a higher Bi ratio could provide more active sites for CO_2 reduction and key intermediate (i.e., *CHO) generation, owing to the lower charge transfer resistance of the BiO_x that can facilitate reduction of CO_2 (Figure S15, Supporting Information). Thus, enhancing Bi ratio offers more opportunity for C—N coupling with $*NH_2$.

Furthermore, in addition to formamide, methylamine (CH_3NH_2) and formaldoxime (CH_3NO) were produced (Figures S16 and S17, Supporting Information), giving a total faradaic efficiency toward C—N products of 7.5 ± 0.8% with the $3CuO_x/7BiO_x$ catalyst at −1.0 V versus RHE (Figure 1f). These products share common intermediates with the formamide.[6b] Increasing the applied potential from −0.8 to −1.0 V versus RHE might overcome the overpotentials associated with the methylamine and formaldoxime production, enhancing their FEs, and thus compete with formamide selectivity.[6b] However, increasing applied potentials >−1.0 V versus RHE leads to a shift in the selectivity toward HER and C_{2+} products (Figure S16a, Supporting Information). At lower Bi:Cu ratios, an upward trend of the faradaic efficiency for the C_{2+} products (i.e., ethanol and 2-propanol) and NH_4^+ was seen, as Cu exhibits activity for NO_2^- to NH_4^+ conversion and *COOH intermediates generation (precursor for C_{2+} products) from CO_2.[2a,7] Thus, Bi addition is very significant in facilitating CO_2 reduction to *CHO (Figure S16a, Supporting Information).

CuO_x/BiO_x was then tested within a two-electrode flow electrolyzer (Figure S18, Supporting Information), employing NO_3^- and NO_2^- as nitrogen sources, while maintaining an optimized catholyte concentration (0.2 M $KHCO_3$ + 0.02 M KNO_x), in line with optimization strategies used in two-compartment cell. Polarization curves show that NO_2^-RR displays earlier activation than NO_3^-RR (Figure S19c, Supporting Information). The ensuing *i–t* curves reveal notably enhanced *j* when NO_2^- was utilized (Figure S19d, Supporting Information), yielding value *ca.* −106 mA cm^{-2} at −3.0 V. In contrast, the *j* of NO_3^- at the same potential reaches *ca.* −76 mA cm^{-2}. These differences highlight the activity of NO_2^- for C–N coupling with a yield rate and FE of 101 ± 18 mmol h^{-1} g_{cat}^{-1} (51 ± 9 μmol h^{-1} cm^{-2}) and 3.30 ± 0.80% at −3.0 V, compared to NO_3^- that has yield rate and FE of 55 ± 11 mmol h^{-1} g_{cat}^{-1} and 2.2 ± 0.63%, respectively (Figure S20a,b, Supporting Information). We also varied reaction time (*t*) between 0.5 and 3 h at −3.0 V (Figure S19a,b, Supporting Information). However, extending *t* > 2 h enhances the FE of C_{2+} products (i.e., ethanol and 2-propanol), potentially attributed to a prolonged period facilitating dimerization of CO_2 intermediates.[28] In attempts to further improve formamide selectivity, we made the alkaline anolyte (0.1 M KOH), while keeping the composition of catholyte unchanged (0.2 M $KHCO_3$ + 0.02 M KNO_x). Our findings revealed that this replacement leads to an enhancement in the *j* to −125 and −90 mA cm^{-2} for NO_2^- and NO_3^- at −3.0 V, respectively (Figure 1g; Figure S19e,f, Supporting Information). The use of KOH solution as anolyte can also reduce overpotentials at anode, improving oxygen evolution reaction (OER) and ionic conductivity in the anode layer.[29] The highest formamide yield rate and FE of 134 ± 11 mmol h^{-1} g_{cat}^{-1} (67 ± 6 μmol h^{-1} cm^{-2}) and 4.8 ± 0.4% were achieved at a cell potential of −3.0 V using NO_2^- as nitrogen source (Figure 1h; Figure S20c, Supporting Information). When KOH serves as the anolyte, the

oxidation of hydroxyl (OH^-) groups in the anode chamber, leading to minimal transfer of H^+ to catholyte chamber (as illustrated in Figure S18c, Supporting Information). This process stabilizes the pH of the catholyte, thereby maintaining relatively stable formate and *CHO intermediates.[30] Furthermore, the restricted migration of H^+ to the cathode chamber suppresses the competitive HER, as displayed in Figure S20d,e (Supporting Information).

The yield rate achieved in this study is the highest yield rate reported to date through co-electroreduction of CO_2 and NO_x^- in a flow electrolyzer system (Table S1, Supporting Information). No other C—N products are identified amidst CO_2RR products, including methanol, ethanol, acetate, and 2-propanol (Figure S20f, Supporting Information). This improved performance is attributed to the overcoming of CO_2 mass transfer limitations, as the electrolyzer configuration intensifies the mass-transport of reactants toward the active sites.[31]

2.3. Characterization of the CuO_x/BiO_x Catalyst

The scanning electron microscopy (SEM) of the (y)CuO_x/(1-y)BiO_x catalysts demonstrates a uniformly porous distribution on the CFP over a large area, as revealed by **Figure 2a** and Figure S21 (Supporting Information). Transmission electron microscopic (TEM) analysis and corresponding energy dispersive X-ray spectroscopic (EDS) elemental mapping (Figure 2b,c; Figures S22 and S23, Supporting Information) display the nanocomposite structure of the blended CuO_x and BiO_x nanoparticles with predominant lattice spacing of 2.3, 2.7, and 3.2 Å corresponds to CuO (111), Bi_2O_3 (400), and Bi_2O_3 (201) planes, respectively.

The X-ray photoelectron spectra (XPS) (Figure 2d,e; Figures S25 and S26, Supporting Information) confirm the presence of all expected elements in the as-prepared catalysts and their states are consistent with the X-ray diffraction (XRD) patterns. The X-ray absorption near edge structure (XANES) and extended X-ray absorption fine structure (EXAFS) at Cu K-edge and Bi L_3-edge (Figures S27 and S28, Supporting Information) are consistent with the CuO and Bi_2O_3 reference for all CuO_x/BiO_x materials examined. No features other than CuO and Bi_2O_3 are seen at apparent distance (*R'*) *ca.* 1.5 and 1.7 Å, respectively, indicating no intermetallic compounds (Figure 2f,g; Figures S27 and S28, Supporting Information). The collective data from XAS, TEM, and XRD analyses suggest that CuO_x and BiO_x form nanocomposites rather than alloys, which can maintain their intrinsic catalytic properties at nanoscales.[32]

Further, we investigated changes to the CuO_x/BiO_x catalysts induced by the electrochemical tests for the CO_2 and NO_3^- co-reduction at −1.2 V versus RHE over 12 h. SEM images indicate that, despite the agglomeration of smaller particles into larger clusters, the porous morphology of the catalysts is largely maintained, as observed in SEM images (Figure S29, Supporting Information). The XPS survey and high-resolution O 1s spectra show a reduction in the intensity of O_I peak (Figures S30 and S31, Supporting Information), attributed to the reduction of metal oxides. The observation of Cu 2p spectra exhibits a shift of the Cu $2p_{3/2}$ peak from 933.6 to 934.5 eV, implying the formation of $Cu(OH)_2$ (Figure 2d), whilst the Cu_{LMM} spectra (Figure S32, Supporting Information) displays two components which are similar to those of $Cu(OH)_2$ and Cu_2O.[33] The high-resolution Bi 4f spectra of post-reaction catalysts (Figure 2e) reveal the unchanged oxidation state of BiO_x.

The Cu K-edge XANES and EXAFS of the post-reaction CuO_x/BiO_x catalyst (Figure 2f; Figure S33a–d, Supporting Information) shift to lower energy and also suggest the formation of Cu_2O and Cu in addition to the initially present CuO.[34] The Bi L_3-edge XANES and EXAFS (Figure 2g; Figure S34a–d, Supporting Information) show characteristics of Bi^{3+} oxide, in line with the XPS results. The ex situ Raman spectra (Figure S35a,b, Supporting Information) also corroborate these results, in which Cu_2O peaks are detected at 215 and 629 cm^{-1} alongside CuO peaks at 263 and 590 cm^{-1},[35] whilst Bi^{3+} oxide peaks manifest at 130 cm^{-1}.[36] From the characterization results, the post-reaction catalyst displays the presence of the $Cu^{2+}/Cu^+/Cu^0$ and Bi^{3+} admixture, implying that CuO_x experiences reduction during the reaction and the propensity for reoxidation of BiO_x upon exposure to air after the reaction is halted (as demonstrated by the in situ Raman measurements discussed below).[1c,37]

2.4. In Situ Investigations of the Active Sites and C–N Coupling Mechanism

To ascertain the active species of the CuO_x/BiO_x catalyst, in situ Raman measurements were undertaken between the range of 100–750 cm^{-1} at −1.0 V versus RHE under different time intervals (**Figure 3a**; Figure S36, Supporting Information). The in situ Raman spectra at open circuit potential (OCP) exhibit distinctive peaks at 288 and 590 cm^{-1}, associated with CuO,[35] and at 130 cm^{-1}, attributed to Bi_2O_3.[36] Upon applying a potential of −1.0 V versus RHE, Cu_2O peaks emerge at 188 and 628 cm^{-1},[38] indicating CuO reduction. As the reaction progresses, the intensity of the Cu_2O peaks diminishes and eventually dissipates after ≈45 min, signifying the reduction of Cu_2O to a metallic state. The Cu_2O peaks re-emerge when the reaction ceases, indicating the reoxidation of metallic Cu into Cu_2O to a certain extent. Additionally, the 130 cm^{-1} peak of Bi^{3+} is substantially reduced soon after the application of the cathodic potential and reappears when the potential is halted. This observation provides evidence that Bi^{3+} undergoes reduction to the Bi^0 state, corroborating findings reported in the literature.[1c,39] Based on the in situ Raman spectra, we conclude that Cu^+/Cu^0 and Bi^0 are the key species on the CuO_x and BiO_x sites, respectively.

In situ Raman spectroscopy was also employed to temporally assess intermediates during the co-electroreduction of CO_2 and NO_2^-. Spectra within the wavenumber range of 950–1800 cm^{-1} were recorded at different time intervals while operating at −1.0 V versus RHE (Figure 3b). Initially, discernible peaks associated with $*HCO_3^-$, $*CO_3^{2-}$, and $*NO_2^-$ are detected at of 1018, 1060, and 1356 cm^{-1}, respectively.[40] The appearance of $*CO_3^-$ peak can be attributed to the saturated CO_2 in the catholyte.[41] As the reaction proceeds, a decline in signals corresponding to $*NO_2^-$ and $*CO_3^{2-}$ is observed, while the stretching mode of C═O bond (*ν* *CO) related to *COOH emerges at 1630 cm^{-1} after ≈8 min.[42] Subsequently, a stretching vibration of the C–N bond ≈1395 cm^{-1} is observed after ≈42 min, implying the formation of formamide on the catalyst surface.[43]

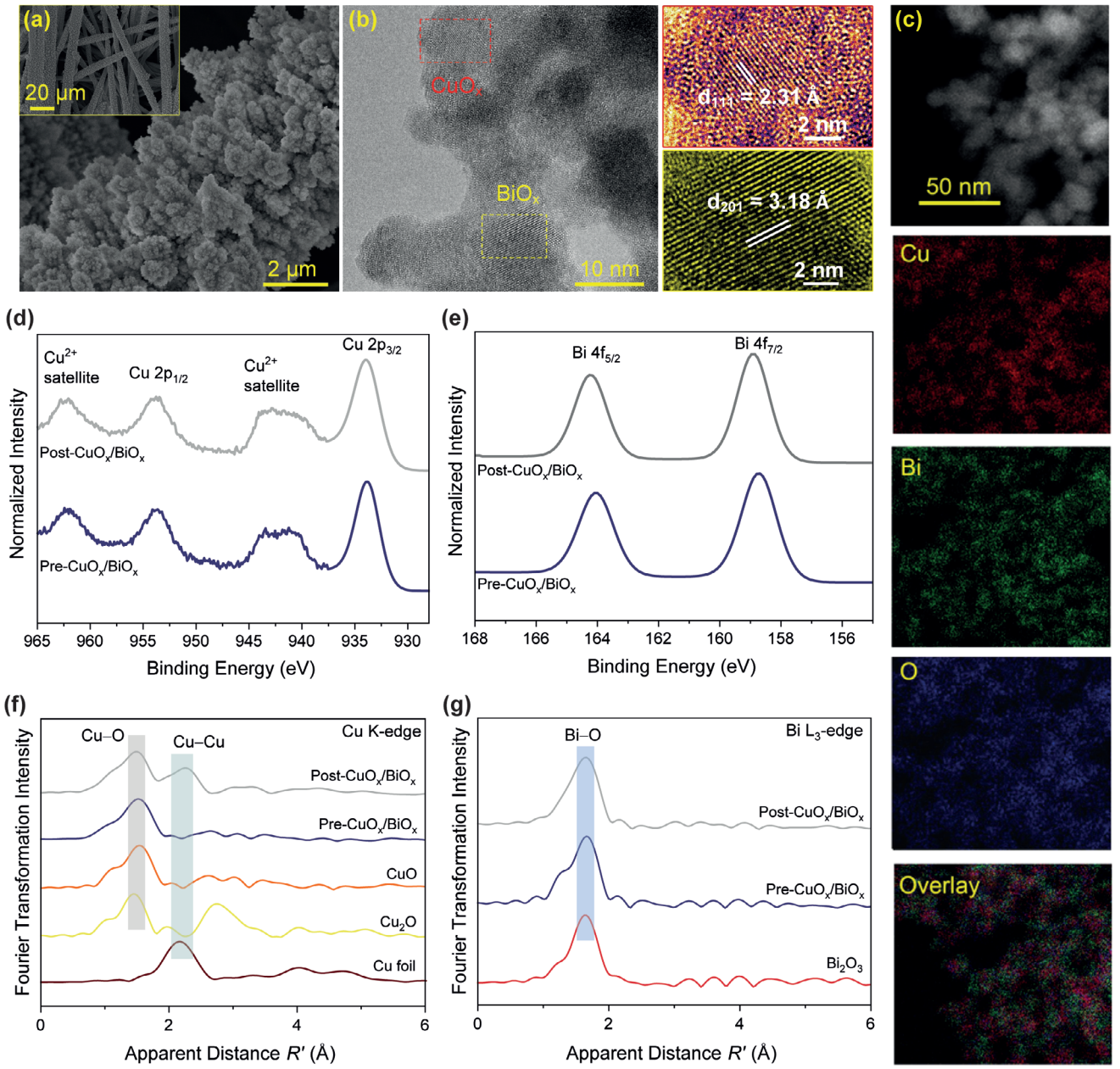

Figure 2. The characterization of CuO_x/BiO_x catalyst: a) SEM, b) TEM, and c) corresponding EDS mapping images of CuO_x/BiO_x. High-resolution XPS spectra for pre- and post-reaction CuO_x/BiO_x catalyst: d) Cu 2p and e) Bi 4f. The FT-EXAFS spectra of pre- and post-reaction CuO_x/BiO_x catalyst: f) The Cu K-edge and g) The Bi L_3-edge. The grey, green, and blue box in panels f-g indicate the peak positions of Cu—O, Cu—Cu, and Bi—O, respectively.

To probe more comprehensive real-time intermediate formation during co-electroreduction of CO_2 and NO_2^-, in situ synchrotron radiation-infrared transmission (SR-FTIR) was performed. The in situ SR-FTIR technique was applied across various applied potentials (−0.8 to −1.2 V vs RHE, Figure 3c–e). At −0.8 V versus RHE, the emergence of *NO stretching, *NH bending (δ_s NH_2), and *NH_2 rocking mode (ρ_s NH_2) at 1957, 3180, and 1153 cm^{-1}, respectively, signifies the adsorption and activation of NO_2^- to *NH_2.[44] Moreover, the detection of *COOH and *HCOO intermediates at 1285 and 1365 cm^{-1} indicates CO_2 adsorption and activation.[45] The *CHO intermediate emerges at 1733 cm^{-1} from −0.8 versus RHE and its vibration intensity increases along with negative applied potentials.[7,23a,46] The infrared band at 1450 cm^{-1} can be assigned to the C–N bond in the formamide, as the characteristic C–N stretch of amides typically manifests within the range of 1435 to 1455 cm^{-1}.[5,7,44,47] Notably, this band reaches its maximum intensity at −1.0 V versus RHE. The in situ SR-FTIR analysis suggests that *NH_2 and *CHO intermediates are the key intermediate for the formation of formamide, which is further confirmed by additional in situ SR-FTIR investigations conducted at different time intervals (Figure S37, Supporting Information).

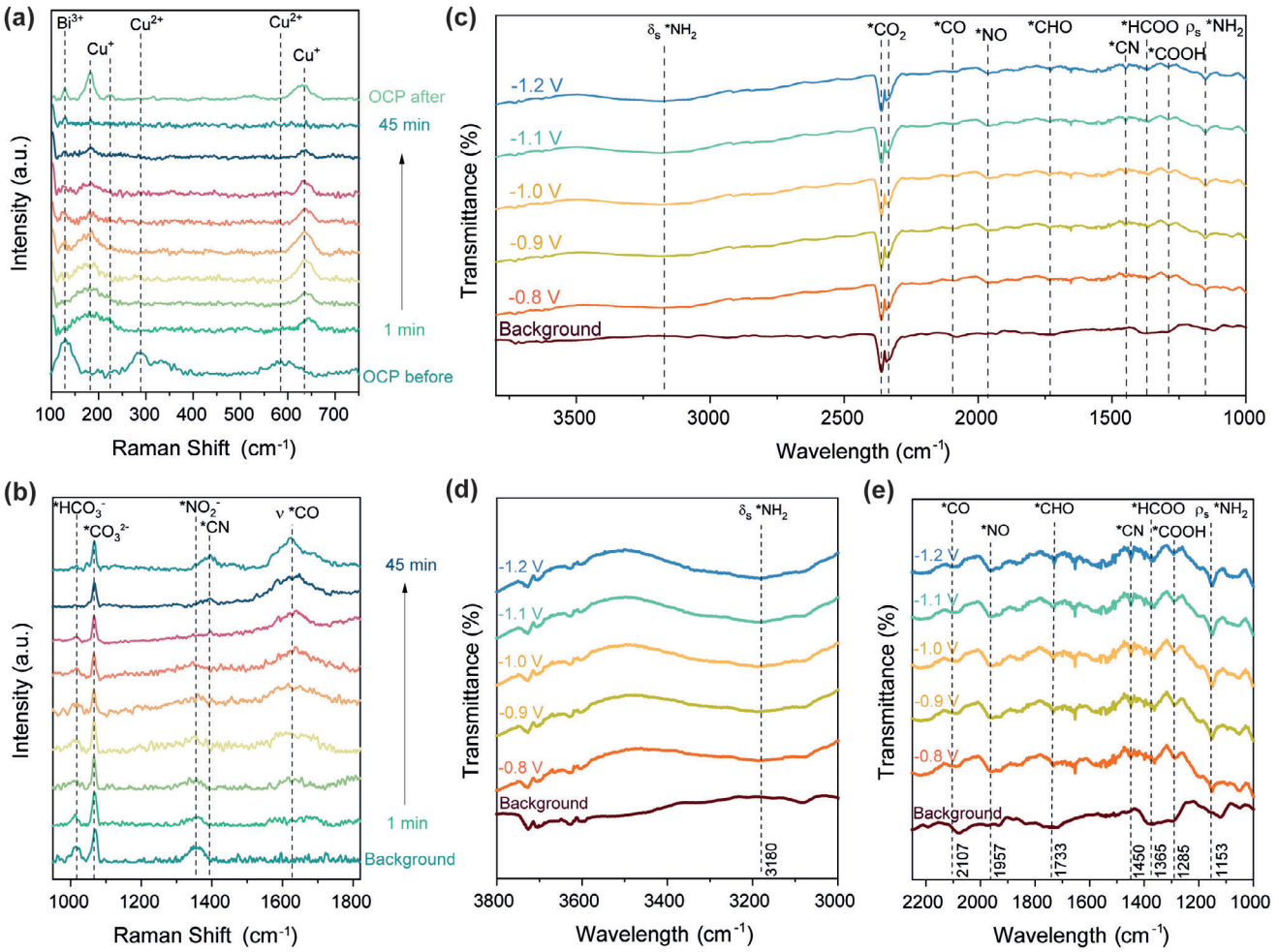

Figure 3. In situ characterization of CuO_x/BiO_x catalyst: The in situ Raman spectroscopy for different time intervals with wavelength window at a) 100–750 cm^{-1} and b) 950–1800 cm^{-1} at −1.0 V versus RHE. c) The in situ SR-FTIR with enlarged wavelength windows at d) 3800–3000 cm^{-1} and e) 1000–2250 cm^{-1}. The potential unit displayed in the in situ SR-FTIR figures is in V versus RHE. All experiments were carried out in CO_2-saturated 0.2 M $KHCO_3$ and 0.02 M KNO_2 solution.

The in situ SR-FTIR analysis on individual CuO_x and BiO_x catalysts provides insight into their respective roles within CuO_x/BiO_x nanocomposite during the co-electroreduction of CO_2 and NO_2^- (Figure S38, Supporting Information). In the case of CuO_x site, we observed distinct infrared bands corresponding to the $*NH_2$ stretching (ν_{as} NH_2), *NH bending, *NO stretching, and $*NH_2$ rocking mode at 3545, 3060, 1957, and 1140 cm^{-1}, respectively.[44] Conversely, the BiO_x exhibits notably weaker intensities in these infrared bands. Furthermore, different CO_2RR pathways are identified on CuO_x and BiO_x materials. The *HCOO intermediate is identified *ca.* 1370 cm^{-1} on CuO_x and BiO_x sites, respectively, signifying CO_2 reduction to formate. The *COOH and *CO signals present on CuO_x (primarily serving as precursors for methanol and ethanol) at 1285 and 2107 cm^{-1}, accordingly.[48] Moreover, the *CHO intermediate is detected on both BiO_x and CuO_x, suggesting that both CO_2RR pathways are capable of forming the intermediate. Notably, the C–N bond signal is discernible at 1455 cm^{-1} on CuO_x site, indicating formamide formation.

2.5. Density Functional Theory Calculation

The in situ Raman spectra show evidence of Cu^+/Cu^0 and Bi^0 admixture throughout the CO_2 and NO_2^- co-electroreduction. Moreover, the in situ SR-FTIR measurements identify *CHO and $*NH_2$ as pivotal intermediates, as well as the distinct trends in generating intermediates on individual CuO_x and BiO_x. Therefore, to probe the roles of Cu^+, Cu^0, and Bi^0, the DFT calculations for the NO_x^-RR, CO_2RR, and C—N coupling (**Figure** 4a–c; Figure S39a–c, Supporting Information) were carried out. The DFT calculations on Bi^{3+} are also presented in Figure S39e,f (Supporting Information) to account for its transient presence during in situ Raman measurements. However, Bi^{3+} was not considered as the main active site due to the weak signals observed during these tests. Additionally, corroborative studies support the notion that Bi^{3+} is reduce to Bi^0 under negative potentials.[1c,39]

The calculated free energies for the CO_2 reduction reaction support the notion that the addition of BiO_x on (y)CuO_x/(1-y)BiO_x catalyst could improve the adsorption of CO_2, owing to a low Gibbs free energy (ΔG) of −2.33 eV (Figure 4a). The subsequent

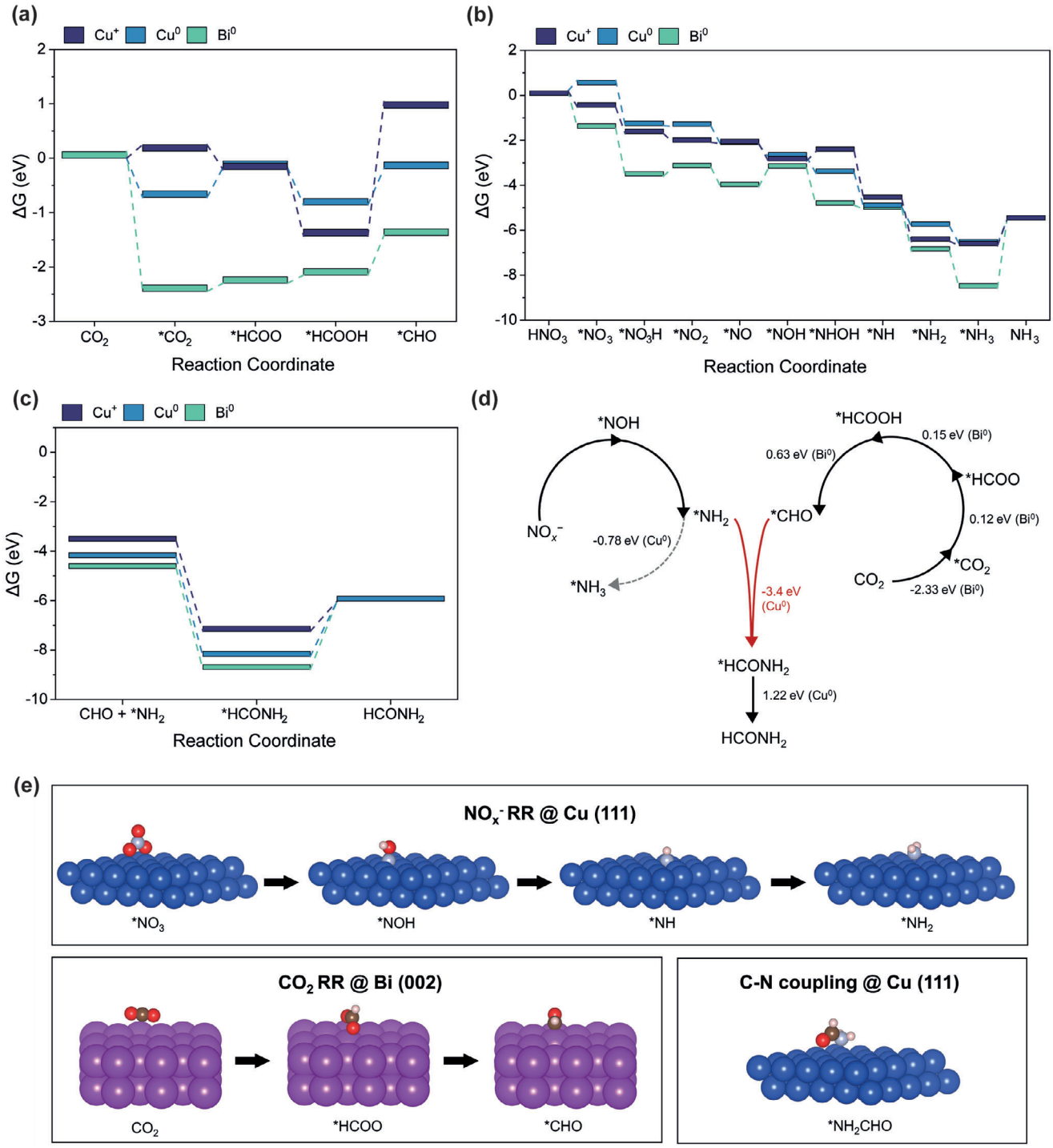

Figure 4. Free density calculated from the DFT on CuO_x/BiO_x catalyst for a) CO_2RR, b) NO_x^-RR, and c) C–N coupling. d) The proposed co-electroreduction of CO_2 and NO_x^- for formamide synthesis on the CuO_x/BiO_x nanocomposite. e) Schematic illustration of formamide generation that shows favorability of $*NH_2$ coupling with *CHO than $*NH_3$ formation by comparing ΔG. f) Molecule configurations with the modeled Cu^0 and Bi^0 structures depict the simplification of NO_3^-RR to $*NH_2$ intermediate, CO_2RR to *CHO intermediate, and formamide synthesis. The blue, purple, red, grey, pink, and brown balls represent Cu, Bi, O, N, H, and C atoms, respectively.

conversion of $*CO_2$ to *CHO can proceed via *COOH ($*CO_2$ → *COOH → *CO → *CHO) and *HCOO ($*CO_2$ → *HCOO → *HCOOH → *CHO) pathways,[49] as displayed in Figure 4a and Figure S39a (Supporting Information). Based on DFT calculations, the CO_2RR is thermodynamically challenging due to positive ΔG for the formation of the intermediates. Cu^+ sites primarily reduce CO_2 to *HCOOH, yet the formation of *CHO is hindered by a large ΔG (2.23 eV). Likewise, Cu^0 sites encounter challenges in the hydrogenation of CO_2 to *COOH and *HCOO, as well as *CHO formation due to uphill ΔG of 0.37, 0.55, and 0.67 eV, respectively. Conversely, Bi^0 sites demonstrate a preference for generating *CHO through the *HCOO pathway. Despite similar upward steps in forming *HCOO, *HCOOH, and *CHO intermediates (ΔG_{*HCOO} = 0.12 eV, ΔG_{*HCOOH} = 0.15 eV, and ΔG_{*CHO} = 0.63 eV), these free energies are comparatively lower than those on Cu^+ and Cu^0. From DFT calculations, we hypothesize that Bi^0 sites are thermodynamically more favorable for CO_2 reduction to *CHO compared to Cu^0 and Cu^+, attributed to lower ΔG for CO_2 adsorption and the formation of *HCOO, *HCOOH, and *CHO. The generation of *CHO can be regarded as the limiting step in the CO_2 reduction process, as indicated by elevated ΔG on all sites.

Further, we investigated the NO_x^- reduction reaction pathways as illustrated in Figure 4b and Figure S39b,c (Supporting Information). Several NO_x^-RR pathways have been proposed,[9b,18c] but we found the selected pathways reflect our experimental results, in line with literature findings.[9b,50] The initial step of NO_x^-RR entails the adsorption of NO_x^- species. Notably, Cu^+ and Bi^0 serve as more favorable sites for NO_3^- adsorption compared to Cu^0, with ΔG of −0.33 and −1.27 eV, respectively. The following reduction reactions of $*NO_3$ to $*NO_2$ occur spontaneously on Cu^+ and Cu^0 sites, whereas the formation of $*NO_2$ requires higher energy on Bi^0 (ΔG = 0.37 eV). In contrast, NO_2^- adsorption is a spontaneous process on all components. Subsequent reactions to the formation of $*NH_3$ intermediate are thermodynamically unfavorable on Cu^+ and Bi^0 sites due to higher ΔG in generating *NHOH and *NOH intermediates with value of 0.43 and 0.82 eV, respectively. The desorption of NH_3 proves to be a challenging process on all materials, specifically Bi^0 (3.03 eV). Further evidence indicates that Bi sites exhibit less activity for NO_x^-RR (as displayed in Figure 1b). On this basis, we propose that Cu^+ and Cu^0 are the main key species for NO_x^-RR. Cu^+ facilitates NO_x^- adsorption, while Cu^0 accelerates reduction reactions of $*NO_x$, in tandem with protonation and electron transfer, culminating in NH_3 generation.

The DFT calculation for the C–N coupling between *CHO and $*NH_2$ was explored (Figure 4c; Figure S39d, Supporting Information). DFT calculations reveal that $*NH_2$ can be either spontaneously reduced to $*NH_3$ or coupled with *CHO. By comparing ΔG of both processes (Figure 4d), the coupling between $*NH_2$ and *CHO is thermodynamically more favorable than $*NH_3$ formation.[7] We hypothesize that either *CHO or $*NH_2$ intermediates diffuse around catalyst surface before eventually couple to form formamide. The coupling process is a relatively spontaneous reaction on all materials. Conversely, the desorption of formamide presents a positive ΔG, with Cu^0 showing a slightly preferable energy associated with this step (1.22 eV) compared to Bi^0 (2.77 eV) and Cu^+ (2.24 eV). Based on the DFT calculations, the formamide electrosynthesis can be obtained through two-step process (Figure 4e): i) the reduction reactions of CO_2 to *CHO as well as NO_x^- to $*NH_2$, and ii) the coupling between *CHO and $*NH_2$ intermediates. These findings are consistent with existing literature;[7] however, the incorporation of dual active sites in the catalyst notably reduces the ΔG required for hydrogenation to $*NH_2$ and *CHO, as well as for the C–N coupling process.

The CuO_x/BiO_x catalyst facilitates the continuous relay of *CHO and $*NH_2$ formation, followed by the subsequent C–N coupling. The two potential determining steps for the overall formamide production process on the CuO_x/BiO_x catalyst include the formation and desorption of *CHO and formamide, accordingly. To further enhance the selectivity of C–N products, it is critical to balance the co-adsorption and activation of carbon and nitrogen sources. Additionally, ensuring proximity of bifunctional active sites is essential for facilitating more effective interactions and reactions between reactants and intermediates.

3. Conclusion

In summary, we have demonstrated a strategy for the co-electroreduction of CO_2 and NO_x^- into formamide. The CuO_x/BiO_x nanocomposite displays C–N coupling capabilities, achieving a maximum formamide yield rate of 134 ± 11 mmol h^{-1} g_{cat}^{-1} in a continuous flow electrolyzer system at an applied potential of −3.0 V (j = 125 mA cm^{-2}). We elucidate the ratio of Cu:Bi in the catalyst, the electrolyte composition, and cell systems play a crucial role in determining the selectivity for CO_2RR, NO_x^-RR, and the C—N coupling process. The $3CuO_x/7BiO_x$ catalyst exhibits the highest yield rate of C—N products in CO_2-saturated 0.2 M $KHCO_3$ and 0.02 M KNO_2 catholyte, attributed to its lower ΔG for CO_2 adsorption, along with available active sites for *CHO and $*NH_2$ formation. Continuous flow electrolyzer system improves the CO_2 mass transfer limitations and intensifies the mass-transport of reactants toward the active sites. Replacing $KHCO_3$ anolyte to KOH in the flow cell system also enhances the formamide selectivity, owing to stable formate and *CHO intermediates, as well as restricted migration of H^+ to suppress HER. In situ Raman spectroscopy reveals a synergy interaction between Cu^+/Cu^0 and Bi^0 that likely contributes to the enhanced C—N coupling performance. Cu^+ facilitates adsorption of NO_x^-, while Cu^0 accelerates subsequent hydrogenation and electron transfer converting $*NO_x^-$ to $*NH_2$. Bi^0 reduces CO_2 adsorption energy and accelerates *CHO formation. Furthermore, in situ SR-FTIR and in situ Raman data provide valuable insights by identifying the key intermediates for C—N coupling. DFT calculations further support and validate the mechanism of formamide generation through the coupling of *CHO and $*NH_2$ intermediates, highlighting a new approach for C—N coupling electrosynthesis through the nanocomposite of *p*-block metal oxides and CuO_x.

4. Experimental Section

Materials: All chemicals utilized in this study were of analytical grade and used as received without any additional purification. Deionized water (resistivity of 18.2 MΩ cm^{-1} at 25 °C) was employed in all experimental procedures.

Catalyst Preparation: All catalysts were prepared using a custom-built FSP system.[51] Typically, Sn, Cu, Bi, and their combination precursors were prepared from mixing Tin(II) 2-ethylhexanoate (99%, Sigma–Aldrich), copper(II) naphthenate in mineral spirits (8% Cu, Strem Chemicals) and/or bismuth(III) 2-ethylhexanoate (70-75% in xylenes, 24% Bi, Strem) were dissolved in a 1:1 (vol) mixture of toluene (anhydrous 99.8%, Sigma–Aldrich) and 2-ethylhexanoic acid (99%, Sigma–Aldrich) to achieve concentrations of 0.2 M for both precursors (total metal precursor concentration). The precursor solution was injected into the FSP system with a volume flow of 5 mL min^{-1} using a syringe pump and atomized with oxygen flow of 5 mL min^{-1} (Coregas, 99.9%). The flame was ignited and maintained with a supporting flame mixture, which consisted of 3.2 L min^{-1} oxygen and 1.5 L min^{-1} methane (Coregas, ≥99.95%). The target oxides were deposited directly on carbon fiber paper within 1 min of deposition. This type of catalyst was used for electrochemical testing in the H-cell system. The powder was also collected at the glass fiber filter for characterization and electrochemical testing in the flow electrolyzer.

Electrochemical Experiments: Electrochemical experiments were initially performed in a three-electrode customized H-cell system with a Nafion 117 membrane (Sigma-Aldrich) to separate the gas-tight working and counter electrode compartments. A platinum plate and saturated calomel electrode (SCE) were utilized as the counter and reference electrodes, respectively. Ar-saturated 0.1 M $KHCO_3$ (99.7%, Sigma–Aldrich) and 0.05 M KNO_3 (≥99%, Sigma–Aldrich), and CO_2-saturated 0.1 M $KHCO_3$ were utilized as the catholyte for the NO_3^-RR and CO_2RR, respectively. The electrocatalytic C—N coupling was initially carried out in the CO_2-saturated 0.1 M $KHCO_3$ and 0.05 M KNO_3 solution. The anolyte for all electrochemical measurements used the same solution as the catholyte but without gas saturation. Prior to testing, the cathodic compartment of the cell was purged with the relevant gas for 20 min, resulting in a pH of 8.34, 6.76, and 6.82 for the NO_x^-RR, CO_2RR and C—N coupling electrosynthesis, respectively. The Ar (Coregas, grade 5) and CO_2 (Coregas, grade 2.5) gases flowrates were maintained at 10 mL min^{-1} (9.4 standard liter per minute (SLPM)) during the NO_x^-RR, CO_2RR, and C—N coupling reaction. Electrochemical measurements were conducted with an Autolab M204 (Metrohm Autolab) electrochemical workstation. Fixed potential electrolysis was then carried out for at least three different measurements and the reported potentials were converted to the reversible hydrogen electrode (RHE) reference for benchmarking with literature using the following equation: E_{RHE} (V) = E_{SCE} (V) + 0.245 + 0.059×pH. The electrical impedance spectroscopy (EIS) was measured at −1.0 V versus RHE in a CO_2-saturated 0.2 M $KHCO_3$ and 0.02 M KNO_2 (≥98%, Chem Supply) solution with the frequency varied from 100 kHz to 0.1 Hz. The EIS fitting was conducted using the ZFit function in ECLab software version 11.42. The two-electrode flow electrolyzer (Figure S18, Supporting Information) system used Ni foam as an anode and a CuO_x/BiO_x as a cathode; both electrodes had a geometric surface area of 1 cm^2. The Nafion membrane was sandwiched between the electrodes. The CO_2 gas flow rate was maintained at 50 mL min^{-1} (47.2 SLPM). Initially the catholyte and anolyte used remained consistent with that employed in H-cell experiments, later the anolyte was changed to 0.1 M KOH (>90%, Sigma–Aldrich) for optimization. The electrolyte continuously circulated into the system with flow rate of 9.5 mL min^{-1} (8.9 SLPM) for 2 h.

Product Quantification: A gas chromatograph (Shimadzu, Model 2010 Plus) equipped with a thermal conductivity detector (TCD) and a flame ionization detector (FID) was utilized to detect gas products (H_2 and CO), with calibration curves provided in Figure S40 (supporting Information). Quantification of the CO_2RR liquid products was carried out using ^{1}H NMR. Approximately 0.63 mL of the catholyte was mixed with 0.07 mL of D_2O (D-99.9%, Cambridge Isotope Laboratories) and analyzed using a 600 MHz ^{1}H 1D liquid NMR spectrometer (Bruker Advance). The water suppression pre-saturation method was applied to measure the 1D ^{1}H spectrum. External standard methods with 10 mmol mL^{-1} sodium acetate (Sigma–Aldrich, ≥99%) was used for quantification. Approximately 0.5 mL of the catholyte was collected for ammonium (NH_4^+) quantification using the Berthelot test.[52] The catholyte was mixed with reagent 1 that consists of 0.4 mL of 1 M sodium hydroxide solution (Sigma–Aldrich, 99.99%), 5 wt.% salicylic acid (Sigma–Aldrich, 99.99%), and 5 wt.% sodium citrates (Sigma–Aldrich, 99.99%). Mixture was then mixed with 0.1 mL reagent 2 that consists of 0.05 M sodium hypochlorite solution (Sigma–Aldrich, 99.99%) and 30 µL reagent 3 that comprises of 1 wt.% sodium nitroferricyanide solution (Sigma–Aldrich, 99.99%). The sample was then sonicated and incubated in the dark at room temperature for 2 h. A Shimadzu UV-3600 UV–vis–NIR spectrophotometer and 1 cm quartz cuvettes were employed to quantify the amount of ammonium with the absorbance reading between 550 and 800 nm wavelengths. The concentration of ammonium was determined using the calibration curve (Figure S41, Supporting Information) constructed based on the analysis of the electrolyte solutions containing known amounts of NH_4Cl. The identification and quantification of formamide and other liquid products in C—N coupling electrosynthesis were conducted using the ^{1}H NMR method following method by Huang et al.[53] Approximately 400 µL liquid sample was mixed with 200 µL DMSO-d_6 solution (D-99.9%, Cambridge Isotope Laboratories), then the solution was tested in a 600 MHz ^{1}H 1D liquid NMR spectrometer (Bruker Advance) equipped by cryoprobe for 512 scans. The 1D ^{1}H spectrum was measured with water suppression excitation sculpting method. External standard method with 10 mmol mL^{-1} disodium maleate solution (Sigma–Aldrich, ≥98%) was used for quantification.

The faradaic efficiency (FE) and yield rate of liquid product were calculated to see the performance of all catalysts using the following equations:

$$\text{FE}\ (\%) = \frac{n \times F \times V_{aq} \times C_{Product}}{Q} \times 100\% \quad (1)$$

where n is number of electron transfers, F is the Faraday constant (96 485.33 C mol^{-1}), V_{aq} is the volume of catholyte solution (L), $C_{Product}$ is the concentration of product (M), and Q is passed charge (C).

$$\text{Yield rate}_{Product}\left(\text{mmol h}^{-1}\text{g}_{cat}^{-1}\right) = \frac{C_{Product} \times V_{aq} \times MW}{t \times A \times \Gamma} \quad (2)$$

where MW is the molecular weight of product, t is duration of the electrolysis (h), A is the geometric surface area of the electrode (cm^2), and Γ is the catalyst loading per geometric surface area of the electrode (g cm^{-2}); $C_{Product}$ for this calculation is expressed in mM.

The faradaic efficiency of gas product was calculated by the equation:

$$\text{FE}\ (\%) = \frac{n \times F \times V_{gas} \times x}{Q} \times 100\% \quad (3)$$

where V_{gas} is the volume of headspace (L), and x is the concentration of the product in the headspace (mol L_{gas}^{-1}).

Material Characterizations: XRD patterns were recorded using a D2 Phaser Bruker instrument with Cu Kα radiation (λ = 1.54 Å) in a scan range of 10°–80° at a scan rate of 1.17 deg min^{-1}. Nanoparticles powder was placed on a zero-diffraction plate (Silicon crystal). XPS analysis was undertaken using a Thermo ESCALAB250Xi spectrometer. Analysis was employed a monochromated Al Kα (energy 1486.68 eV) source, operated at a power of 120 W (13.8 kV × 8.7 mA), and a hemispherical analyzer functioning in a fixed analyzer transmission mode. The overall pressure in the main vacuum chamber was typically ranged between 10^{-9} and 10^{-8} mbar. Survey spectra were obtained at a pass energy of 100 eV, while high resolution spectra were recorded for individual peaks at pass energy of 20 eV pass energy. The photoelectron take-off angle is 90° with spot size ≈500 µm. Data processing was performed using the ThermoScientific Avantage processing software. The identification of all present elements was conducted from survey spectra. Atomic concentrations of the identified elements were determined using integral peak intensities and sensitivity factors provided by the manufacturer. Binding energies were referenced to the C 1s peak at 284.8 eV (aliphatic hydrocarbon). Quantitative XPS accuracy is estimated to be around 10–15%, and precision, reflecting reproducibility, typically exceeds 5%, a parameter relevant when

comparing similar samples. The morphology was examined using a field-emission scanning electron microscopy (FESEM) Zeiss Ultraplus operating at 3 kV at a working distance of 3 cm without coating and a high-resolution TEM JEOL 2100F operating at 200 kV. For SEM analysis, the electrode cut pieces were affixed onto the specimen stubs using carbon tape. To prepare samples for TEM, the material was carefully scraped from the surface of the electrode and dispersed onto holey carbon-coated nickel grids with a mesh size of 200. Elemental mapping was obtained using a JEOL SDD energy-dispersive X-ray spectrometer coupled with JEOL 2100F, operated at 200 kV. The ex situ Raman measurements were recorded on an inVia Raman spectrometer system (HR Micro Raman spectrometer, Horiba JOBIN YVON US/ HR800 UV) with a wavelength laser of 633 nm. XAS spectra at the Cu K-edge and Bi L_3-edge spectra were obtained using the multipole wiggler XAS beamline 12 ID at the Australian Synchrotron ANSTO, operating on mode 2. The beam energy and current were 3.0 GeV and 200 mA, respectively. Powders data were acquired using fluorescence detection. Cu foil, CuO, Cu_2O, and Bi_2O_3 were used as reference samples. XAS data were analyzed using a combination of *Sakura* for data conversion, *Pyspline* for background subtractions, and *Artemis* for EXAFS fitting.

In Situ Measurements: The operando SR-FTIR measurements were carried out at the Australian Synchrotron ANSTO using a SR-FTIR setup equipped with a ZnSe crystal as the infrared transmission window (cut-off energy 625 cm^{-1}). An infrared microscope (Bruker Hyperion 3000 with an x20 objective) was coupled with an FTIR spectrometer (Bruker 70 v/s) equipped with a KBr beam splitter and liquid-nitrogen-cooled mercury cadmium telluride detector. The catalyst electrode was closely pressed against the ZnSe crystal window with a micrometer-scale gap to minimize the infrared light loss. To ensure the integrity of the acquired SR-FTIR spectra, the apparatus operated in reflection mode with vertical infrared light incidence. Each infrared absorption spectrum was generated by averaging 256 scans at a resolution of 2 cm^{-1}. Prior to each systematic measurement, the background spectrum of the catalyst electrode was obtained at an open-circuit voltage. The potential range for the electroreduction reaction was set at −0.8, −0.9, −1.0, −1.1, and −1.2 V versus RHE with CO_2-saturated 0.2 M $KHCO_3$ and 0.02 M KNO_2 as catholyte. Figure S42b,c (Supporting Information) depicts the in situ electrochemical cell and setup configuration. The in situ Raman measurements were recorded on an inVia Raman spectrometer system (HR Micro Raman spectrometer, Horiba JOBIN YVON US/ HR800 UV) using a spectroelectrochemical Raman cell (Figure S42a, Supporting Information). The Raman cell was operated with a 633 nm argon ion laser and equipped with a reference electrode of Ag/AgCl and a counter electrode of Pt wire. The cell was filled with an electrolyte solution consisting of CO_2-saturated 0.2 M $KHCO_3$ and 0.02 M KNO_2 and connected to an Autolab potentiostat (PGSTAT204) to simulate electrocatalytic C–N coupling.

Density Functional Theory Calculations: The DFT calculations were performed using the Projector Augmented Wave (PAW) method[54] as implemented in the Vienna Ab initio Simulation Package (VASP).[55] The calculations were completed with a plane-wave cut-off energy of 500 eV and Gamma *k*-points mesh of 5 × 5 × 1. The electronic self-consistent calculation was converged to 1×10^{-5} eV and ionic relaxation steps were performed using the conjugate-gradient method (IBRION = 2) and continued until the total force on each atom dropped below a tolerance of −0.025 eVÅ^{-1}. The generalized gradient approximation (GGA) was used for the exchange-correlation functionals as parameterized by Perdew–Burke–Ernzerhof (PBE).[56] The slab models of (2 × 2) Cu (111) surface with 6.21 Å thickness, (2 × 2) CuO (110) surface with 5.74 Å thickness, (2 × 2) Cu_2O (111) surface with 6.26 Å thickness, (2 × 2) Bi (002) surface with 9.71 Å thickness and (1 × 1) Bi_2O_3 (201) surface with 5.00 Å thickness were used. A vacuum thickness of 15 Å in the z-direction was used for relaxation. Bulk-surface interaction was introduced by relaxing only atoms in the two uppermost layers and fixing atoms in other layers to their bulk coordinates. Free energy diagrams were calculated by including the correction of entropy and zero-point energy for CO, CO_2, H_2O, and H_2. The dispersion correction was also included in this study by using DFT D-3 method.[57]

Supporting Information

Supporting Information is available from the Wiley Online Library or from the author.

Acknowledgements

The work was supported by the Australian Research Council (ARC) Training Centre for The Global Hydrogen Economy. Some parts of this research were undertaken at an infrared (IR) beamline of the Australian Synchrotron, part of ANSTO, NMR Facility within the Mark Wainwright Analytical Centre (MWAC) at the University of New South Wales, the surface analysis laboratory (SSEAU, MWAC), and at the spectroscopy laboratory (SPECLAB, MWAC) for the in situ Raman spectroscopy. The authors acknowledge the grant (AS2023-3/IRM/20397) for synchrotron IR beamtime at the Australian Synchrotron and thank Dr. Jitraporn Vongsvivut, Michael Gunawan, and Zhou Shujie for their supports and assistances with the in situ synchrotron (SR)-FTIR. P.R. acknowledges support from the Indonesian Finance Ministry for Indonesian Endowment Fund for Education (LPDP) scholarship. R.D. and A.N.S. acknowledge support from the ARC through the Discovery Early Career Researcher Award (DE230101396) and the Future Fellowship (FF200100317), respectively. R.D. acknowledges UNSW Scientia Fellowship.

Open access publishing facilitated by University of New South Wales, as part of the Wiley - University of New South Wales agreement via the Council of Australian University Librarians.

Conflict of Interest

The authors declare no conflict of interest.

Author Contributions

R.D., and R.A. conceived the idea and directed the research. P.R. carried out characterization, activity testing, and product quantification. T.K.A.N., T.T.-P., and P.R. conducted material synthesis and characterization. C.H. carried out the in situ SR-FTIR. Z.M. and P.R. carried out the in situ Raman spectroscopy. T.T-P and R.K.H. carried out synchrotron measurements and analysis. P.K. and J.A.Y. carried out density functional theory calculations. P.R., T.T.-P., J.L., J.A.Y., R.K.H., R.D., A.N.S., and R.A. cowrote the paper. All authors contributed to analyzing results and discussion.

Data Availability Statement

The data that support the findings of this study are available from the corresponding author upon reasonable request.

Keywords

electrocatalytic C–N coupling, formamide, metal oxides, nanocomposite

Received: April 21, 2024
Revised: May 8, 2024
Published online: May 23, 2024

[1] a) L. Li, A. Ozden, S. Guo, F. P. Garcıá de Arquer, C. Wang, M. Zhang, J. Zhang, H. Jiang, W. Wang, H. Dong, D. Sinton, E. H. Sargent, M. Zhong, *Nat. Commun.* **2021**, *12*, 5223; b) R. Daiyan, W. H. Saputera, H. Masood, J. Leverett, X. Lu, R. Amal, *Adv. Energy Mater.* **2020**, *10*, 1902106; c) T. Tran-Phu, R. Daiyan, Z. Fusco, Z. Ma, L. R. A. Rahim, A. Kiy, P. Kluth, X. Guo, Y. Zhu, H. Chen, R. Amal, A. Tricoli, *J. Mater. Chem. A* **2020**, *8*, 11233.

[2] a) W. Liu, P. Zhai, A. Li, B. Wei, K. Si, Y. Wei, X. Wang, G. Zhu, Q. Chen, X. Gu, R. Zhang, W. Zhou, Y. Gong, *Nat. Commun.* **2022**, *50*, e13; b) H. Xu, D. Rebollar, H. He, L. Chong, Y. Liu, C. Liu, C.-J. Sun, T. Li, J. V. Muntean, R. E. Winans, D.-J. Liu, T. Xu, *Nat. Energy* **2020**, *5*, 623.
[3] a) X. Song, S. Jia, L. Xu, J. Feng, L. He, X. Sun, B. Han, *Mater. Today Sustainability* **2022**, *19*, 100179; b) J. Li, Y. Zhang, K. Kuruvinashetti, N. Kornienko, *Nat. Rev. Chem.* **2022**, *6*, 303.
[4] a) *Fortune Business Insight* **2024**, *2022*, https://www.fortunebusinessinsights.com/amines-market-106578; b) *B. R. A. Marketing* **2023**, *2023*, https://www.globenewswire.com/en/news-release/2023/03/02/2619432/0/en/Global-Fertilizer-market-is-anticipated-to-grow-steadily-at-a-CAGR-of-5-12-to-be-valued-at-USD-268-44-Billion-Bonafide-Research.html#:~:text=Global%20Fertilizer%20market%20is%20anticipated%20to%20grow%20steadily,challenges%20posed%20by%20soil%20degradation%20and%20climate%20change; c) *Maximize Market Research* **2024**, *2023*, https://www.maximizemarketresearch.com/market-report/acetamide-mea-market/146539/.
[5] J. Li, N. Kornienko, *Chem. Sci.* **2022**, *13*, 3957.
[6] a) Z. Tao, Y. Wu, Z. Wu, B. Shang, C. Rooney, H. Wang, *J. Energy Chem.* **2022**, *65*, 367; b) Y. Wu, Z. Jiang, Z. Lin, Y. Liang, H. Wang, *Nat. Sustainability* **2021**, *4*, 725.
[7] C. Guo, W. Zhou, X. Lan, Y. Wang, T. Li, S. Han, Y. Yu, B. Zhang, *J. Am. Chem. Soc.* **2022**, *144*, 16006.
[8] C. D. Lv, C. Lee, L. X. Zhong, H. J. Liu, J. W. Liu, L. Yang, C. S. Yan, W. Yu, H. H. Hng, Z. M. Qi, L. Song, S. Z. Li, K. P. Loh, Q. Y. Yan, G. H. Yu, *ACS Nano* **2022**, *16*, 8213.
[9] a) X. R. Zhang, X. R. Zhu, S. W. Bo, C. Chen, M. Y. Qiu, X. X. Wei, N. H. He, C. Xie, W. Chen, J. Y. Zheng, P. S. Chen, S. P. Jiang, Y. F. Li, Q. H. Liu, S. Y. Wang, *Nat. Commun.* **2022**, *13*, 5337; b) J. Leverett, T. Tran-Phu, J. A. Yuwono, P. Kumar, C. Kim, Q. F. Zhai, C. Han, J. T. Qu, J. Cairney, A. N. Simonov, R. K. Hocking, L. M. Dai, R. Daiyan, R. Amal, *Adv. Energy Mater.* **2022**, *12*, 2201500.
[10] M. Yuan, H. Zhang, Y. Xu, R. Liu, R. Wang, T. Zhao, J. Zhang, Z. Liu, H. He, C. Yang, S. Zhang, G. Zhang, *Chem. Catalysis* **2022**, *2*, 309.
[11] a) Y. Zhao, Y. Ding, W. Li, C. Liu, Y. Li, Z. Zhao, Y. Shan, F. Li, L. Sun, F. Li, *Nat. Commun.* **2023**, *14*, 4491; b) J. Lan, Z. Wei, Y.-R. Lu, D. Chen, S. Zhao, T.-S. Chan, Y. Tan, *Nat. Commun.* **2023**, *14*, 2870.
[12] J.-Q. Chen, X.-X. Ye, D. Zhou, Y.-X. Chen, *J. Phys. Chem. C* **2023**, *127*, 2918.
[13] M. Xu, F. Wu, Y. Zhang, Y. Yao, G. Zhu, X. Li, L. Chen, G. Jia, X. Wu, Y. Huang, P. Gao, W. Ye, *Nat. Commun.* **2023**, *620*, S14.
[14] M. Jouny, J.-J. Lv, T. Cheng, B. H. Ko, J.-J. Zhu, W. A. Goddard, F. Jiao, *Nat. Chem.* **2019**, *11*, 846.
[15] Y. Luo, K. Xie, P. Ou, C. Lavallais, T. Peng, Z. Chen, Z. Zhang, N. Wang, X.-Y. Li, I. Grigioni, B. Liu, D. Sinton, J. B. Dunn, E. H. Sargent, *Nat. Catal.* **2023**, *6*, 939.
[16] F. D. Speck, S. Cherevko, *Electrochem. Commun.* **2020**, *115*, 106739.
[17] a) S. L. Liu, S. L. Yin, Z. Q. Wang, Y. Xu, X. N. Li, L. Wang, H. J. Wang, *Cell Rep. Phys. Sci.* **2022**, *3*, 100869; b) J. Qin, N. Liu, L. Chen, K. Wu, Q. Zhao, B. Liu, Z. Ye, *Acs Sustainable Chem. Eng.* **2022**, *10*, 15869; c) S. Fu, K. Chu, M. Guo, Z. Wu, Y. Wang, J. Yang, F. Lai, T. Liu, *Chem. Commun.* **2023**, *59*, 4344; d) S. Zhang, J. Geng, Z. Zhao, M. Jin, W. Li, Y. Ye, K. Li, G. Wang, Y. Zhang, H. Yin, H. Zhang, H. Zhao, *EES Catal.* **2023**, *3*, 100869.
[18] a) W. Ma, S. Xie, X.-G. Zhang, F. Sun, J. Kang, Z. Jiang, Q. Zhang, D.-Y. Wu, Y. Wang, *Nat. Commun.* **2019**, *10*, 892; b) T. Tran-Phu, R. Daiyan, Z. Fusco, Z. Ma, R. Amal, A. Tricoli, *Adv. Funct. Mater.* **2019**, *30*, 1906478; c) R. Daiyan, T. Tran-Phu, P. Kumar, K. Iputera, Z. Z. Tong, J. Leverett, M. H. A. Khan, A. A. Esmailpour, A. Jalili, M. Lim, A. Tricoli, R. S. Liu, X. Y. Lu, E. Lovell, R. Amal, *Energy Environ. Sci.* **2021**, *14*, 3588.
[19] a) C. Dai, Y. Qiu, Y. He, Q. Zhang, R. Liu, J. Du, C. Tao, *New J. Chem.* **2019**, *43*, 3493; b) S. Trasatti, *J. Electroanal. Chem. Interfacial Electrochem.* **1972**, *39*, 163.
[20] R. Daiyan, X. Lu, W. H. Saputera, Y. H. Ng, R. Amal, *Acs Sustainable Chem. Eng.* **2018**, *6*, 1670.
[21] J. Wang, J. Zou, X. Hu, S. Ning, X. Wang, X. Kang, S. Chen, *J. Mater. Chem. A* **2019**, *7*, 27514.
[22] a) A. Manzo-Robledo, C. Lévy-Clément, N. Alonso-Vante, *Electrochim. Acta* **2014**, *117*, 420; b) K. Guo, H. Lei, X. Li, Z. Zhang, Y. Wang, H. Guo, W. Zhang, R. Cao, *Chin. J. Catal.* **2021**, *42*, 1439.
[23] a) S. Zhu, B. Jiang, W.-B. Cai, M. Shao, *J. Am. Chem. Soc.* **2017**, *139*, 15664; b) G. A. El-Nagar, F. Haun, S. Gupta, S. Stojkovikj, M. T. Mayer, *Nat. Commun.* **2023**, *14*, 2062.
[24] a) M. C. O. Monteiro, F. Dattila, B. Hagedoorn, R. García-Muelas, N. López, M. T. M. Koper, *Nat. Catal.* **2021**, *4*, 654; b) G. Marcandalli, M. C. O. Monteiro, A. Goyal, M. T. M. Koper, *Accounts Chem. Res.* **2022**, *55*, 1900.
[25] G. Marcandalli, K. Boterman, M. T. M. Koper, *J. Catal.* **2022**, *405*, 346.
[26] a) Y. Wang, W. Zhou, R. Jia, Y. Yu, B. Zhang, *Angew. Chem., Int. Ed.* **2020**, *59*, 5350; b) M. T. de Groot, M. T. M. Koper, *J. Electroanal. Chem.* **2004**, *562*, 81; c) S. Garcia-Segura, M. Lanzarini-Lopes, K. Hristovski, P. Westerhoff, *Appl. Catal., B* **2018**, *236*, 546.
[27] a) H. Xu, Y. Ma, J. Chen, W.-x. Zhang, J. Yang, *Chem. Soc. Rev.* **2022**, *51*, 2710; b) E. Murphy, Y. Liu, I. Matanovic, M. Rüscher, Y. Huang, A. Ly, S. Guo, W. Zang, X. Yan, A. Martini, J. Timoshenko, B. R. Cuenya, I. V. Zenyuk, X. Pan, E. D. Spoerke, P. Atanassov, *Nat. Commun.* **2023**, *14*, 4554.
[28] W. Deng, P. Zhang, Y. Qiao, G. Kastlunger, N. Govindarajan, A. Xu, I. Chorkendorff, B. Seger, J. Gong, *Nat. Commun.* **2024**, *15*, 892.
[29] a) P. Mardle, S. Cassegrain, F. Habibzadeh, Z. Shi, S. Holdcroft, *J. Phys. Chem. C* **2021**, *125*, 25446; b) S. Ghoshal, B. S. Pivovar, S. M. Alia, *J. Power Sources* **2021**, *488*, 229433; c) J. C. Fornaciari, L.-C. Weng, S. M. Alia, C. Zhan, T. A. Pham, A. T. Bell, T. Ogitsu, N. Danilovic, A. Z. Weber, *Electrochim. Acta* **2022**, *405*, 139810.
[30] H. Jiang, L. Wang, B. Gao, Y. Li, Y. Guo, M. Zhuo, K. Sun, B. Lu, M. Jia, X. Yu, H. Wang, Y. Li, *Chem. Eng. J.* **2021**, *422*, 129923.
[31] S. Liang, N. Altaf, L. Huang, Y. Gao, Q. Wang, *J. CO2 Util.* **2020**, *35*, 90.
[32] B. V. Kerr, H. J. King, C. F. Garibello, P. R. Dissanayake, A. N. Simonov, B. Johannessen, D. S. Eldridge, R. K. Hocking, *Energy Fuels* **2022**, *36*, 2369.
[33] M. C. Biesinger, *Surf. Interface Anal.* **2017**, *49*, 1325.
[34] A. Sharma, M. Varshney, J. Park, T.-K. Ha, K.-H. Chae, H.-J. Shin, *RSC Adv.* **2015**, *5*, 21762.
[35] C.-J. Chang, C.-W. Lai, W.-C. Jiang, Y.-S. Li, C. Choi, H.-C. Yu, S.-J. Chen, Y. Choi, *Coatings* **2022**, *12*, 1206.
[36] O. Depablos-Rivera, A. Martínez, S. E. Rodil, *J. Alloy Compd.* **2021**, *853*, 157245.
[37] L. Hu, J. A. Wrubel, C. M. Baez-Cotto, F. Intia, J. H. Park, A. J. Kropf, N. Kariuki, Z. Huang, A. Farghaly, L. Amichi, P. Saha, L. Tao, D. A. Cullen, D. J. Myers, M. S. Ferrandon, K. C. Neyerlin, *Nat. Commun.* **2023**, *14*, 7605.
[38] Y. Deng, A. D. Handoko, Y. Du, S. Xi, B. S. Yeo, *ACS Catal.* **2016**, *6*, 2473.
[39] a) X. Feng, H. Zou, R. Zheng, W. Wei, R. Wang, W. Zou, G. Lim, J. Hong, L. Duan, H. Chen, *Nano Lett.* **2022**, *22*, 1656; b) B. Ávila-Bolívar, M. Lopez Luna, F. Yang, A. Yoon, V. Montiel, J. Solla-Gullón, S. W. Chee, B. Roldan Cuenya, *Acs Appl. Mater. Interface* **2024**, *16*, 11552.
[40] a) J. D. Frantz, *Chem. Geol.* **1998**, *152*, 211; b) P. Singh, M. K. Singh, Y. R. Beg, G. R. Nishad, *Talanta* **2019**, *191*, 364.
[41] T. Loerting, C. Tautermann, R. T. Kroemer, I. Kohl, A. Hallbrucker, E. Mayer, K. R. Liedl, *Angew. Chem., Int. Ed.* **2000**, *39*, 891.

[42] W. Shan, R. Liu, H. Zhao, Z. He, Y. Lai, S. Li, G. He, J. Liu, *ACS Nano* **2020**, *14*, 11363.
[43] Z. Tao, Z. Wu, Y. Wu, H. Wang, *ACS Catal.* **2020**, *10*, 9271.
[44] C. D. Lv, L. X. Zhong, H. J. Liu, Z. W. Fang, C. S. Yan, M. X. Chen, Y. Kong, C. Lee, D. B. Liu, S. Z. Li, J. W. Liu, S. Li, G. Chen, Q. Y. Yan, G. H. Yu, *Nat. Sustainability* **2021**, *4*, 868.
[45] a) N. N. Meng, Y. M. Huang, Y. Liu, Y. F. Yu, B. Zhang, *Cell Rep. Phys. Sci.* **2021**, *2*, 100378; b) T. Zheng, C. Liu, C. Guo, M. Zhang, X. Li, Q. Jiang, W. Xue, H. Li, A. Li, C.-W. Pao, J. Xiao, C. Xia, J. Zeng, *Nat. Nanotechnol.* **2021**, *16*, 1386.
[46] A. Wuttig, C. Liu, Q. Peng, M. Yaguchi, C. H. Hendon, K. Motobayashi, S. Ye, M. Osawa, Y. Surendranath, *ACS Cent. Sci.* **2016**, *2*, 522.
[47] S. Kuang, T. Xiao, H. Chi, J. Liu, C. Mu, H. Liu, S. Wang, Y. Yu, T. J. Meyer, S. Zhang, X. Ma, *Angew. Chem., Int. Ed.* **2024**, *63*, 202316772.
[48] N. N. Meng, X. M. Ma, C. H. Wang, Y. T. Wang, R. Yang, J. Shao, Y. M. Huang, Y. Xu, B. Zhang, Y. F. Yu, *ACS Nano* **2022**, *16*, 9095.
[49] a) C. Yang, Y. Wang, L. Qian, A. M. Al-Enizi, L. Zhang, G. Zheng, *Acs Appl. Energy Mater.* **2021**, *4*, 1034; b) Y. Wang, P. Han, X. Lv, L. Zhang, G. Zheng, *Joule* **2018**, *2*, 2551.
[50] N. Zhang, J. Shang, X. Deng, L. Cai, R. Long, Y. Xiong, Y. Chai, *ACS Nano* **2022**, *16*, 4795.
[51] T. Tran-Phu, R. Daiyan, X. M. C. Ta, R. Amal, A. Tricoli, *Adv. Funct. Mater.* **2021**, *32*, 2110020.
[52] Y. Zhao, R. Shi, X. Bian, C. Zhou, Y. Zhao, S. Zhang, F. Wu, G. I. N. Waterhouse, L. Z. Wu, C. H. Tung, T. Zhang, *Adv. Sci.* **2019**, *6*, 1802109.
[53] Y. M. Huang, Y. T. Wang, L. Y., A. J. Ma, J. Z. Gui, C. X. Zhang, Y. F. Yu, B. Zhang, *Chem. Eng.* **2023**, *453*, 1.
[54] a) P. E. Blöchl, *Phys. Rev. B* **1994**, *50*, 17953; b) G. Kresse, D. Joubert, *Phys. Rev. B* **1999**, *59*, 1758.
[55] a) G. Kresse, J. Furthmüller, *Comput. Mater. Sci.* **1996**, *6*, 15; b) G. Kresse, J. Furthmüller, *Phys. Rev. B* **1996**, *54*, 11169.
[56] J. P. Perdew, K. Burke, M. Ernzerhof, *Phys. Rev. Lett.* **1996**, *77*, 3865.
[57] S. Grimme, J. Antony, S. Ehrlich, H. Krieg, *J. Chem. Phys.* **2010**, *132*, 154104.